

BREAK OUT OF A-76 ICEBERG AND RECENT DYNAMIC CHANGES OF ITS ENCOLSURE RIFTS IN RONNE ICE SHELF, ANTARCTICA

A. Zhao^{1,2}, Y. Cheng^{1,2*}, D. Lv^{1,2}, M. Xia^{1,2}, R. Li^{1,2*}, L. An^{1,2*}, S. Liu^{1,2}, Y. Tian^{1,2}

¹ College of Surveying and Geo-Informatics, Tongji University, 1239 Siping Road, Shanghai, China

² Centre for Spatial Information Science and Sustainable Development Applications, Tongji University, 1239 Siping Road, Shanghai, China

(zhaoaiguo, chengyuan_1994, lvda, menglianxia, anlu2021, liusjtj, tianyixiang) @tongji.edu.cn; ronli_282@hotmail.com

Commission III, WG III/9

KEY WORDS: Ronne Ice Shelf, Iceberg Calving, Rift, Satellite Observation

ABSTRACT:

Monitoring the stability of the Ronne Ice Shelf, particularly the calving event, is an integral and important part of the study of Antarctic ice sheet mass balance and sea-level rise. This paper presents the results of the analysis of the world's largest iceberg (A-76 iceberg), which was formed during a calving event in the Ronne Ice Shelf (RIS) on May 13, 2020, and subsequently broke into three fragments (A-76A, A-76B, and A-76C icebergs). The iceberg development cycle, up to this point, including its formation, separation and drift, was observed and analyzed. The detailed development process of rifts associated with the detachment of the A-76 iceberg in front of RIS before calving was analyzed using remote sensing data from multiple sources (ERS, RADARSAT-1, ALOS PALSAR, Landsat-7, and Landsat-8). In addition, based on a total of 66 Sentinel-1 A/B Synthetic Aperture Radar (SAR) images acquired between May 13, 2021 and March 11, 2022, a multi-scale segmentation approach was applied to continuously track the drift path of A-76 icebergs, A-76A, A-76B, and A-76C. We calculated the average drift velocity of these icebergs and found that A-76C iceberg drifted the fastest, followed by A-76A, and A-76B, from May 30, 2021, to March 11, 2022. Future tracking of other iceberg parameters, such as area, thickness, freeboard, and volume, could help assess the melting rates of the icebergs.

1. INTRODUCTION

The Antarctic Ice Sheet (AIS) is one of the most vulnerable and critical regions under the influence of global climate change, and its mass balance will significantly affect global sea level rise. Complete melting of the AIS would result in global sea level rise of ~57.9m (Morlighem et al., 2020). Two pathways by which lost Antarctic mass enters the Southern Ocean are calving at ice shelves and basal melting, each accounting for about half of the total mass loss (Paolo et al., 2015; Rignot et al., 2013). Monitoring accelerated ice shelf thinning and calving processes is essential to quantify ice shelf instability and assess the contribution of AIS to global sea level rise. In addition, an increasing number of calving events or accelerated ice shelf thinning could destabilize ice shelves and lead to a reduction in ice shelf support for the entire ice sheet (Gudmundsson, 2013).

In recent decades, many studies have been conducted on the calving processes of ice shelves at AIS, including the Amery Ice Shelf (Fricker et al., 2005), the Larsen C Ice Shelf (Larour et al., 2021), the Brunt Ice Shelf (Cheng et al., 2021), and others. However, research on calving in the Ronne Ice Shelf (RIS) is not as extensive. The Filchner-Ronne Ice Shelf (FRIS) in the southern Weddell Sea accounts for 30% (~430 000 km²) of the total area of AIS, and the amount of ice stored in its upstream drainage basins has the potential to raise sea level by ~14 m (Morlighem et al., 2020). Using remote sensing datasets from multiple sources (Landsat-7 ETM+, Landsat-8 OLI, Envisat ASAR, ZY-3, WV-2, ICESat), Li et al. (2017) indicated that there are two rapidly developing transverse rifts T1 and T2 on the Filchner Ice Shelf front, which could cause a major calving event

similar to the 1980s. On the other hand, the rifts in the RIS are particularly active in the shelf front region, especially in the two marginal areas and in the frontal calving area. The transverse rifts on the front of the RIS originate from the upstream grounding zone and propagate during their advection process (Hulbe et al., 2010; Walker et al., 2013, 2019). These transverse rifts, together with margin rifts, eventually form plains that are calved into tabular icebergs (Hulbe et al., 2010; Walker et al., 2015; Li et al., 2017). Therefore, studying the evolution of these iceberg-forming rifts can help understand the relationship between shelf stability and calving events in RIS.

Icebergs have a life expectancy of several years or more. Their size ranges from a few square kilometers to several thousand square kilometers. Because icebergs drift with ocean currents, their tracks are a good indicator of ocean circulation (Collares et al., 2018). In addition, drifting icebergs can endanger shipping and affect the marine environment around them (Lasserre, 2015). Therefore, it is important to detect and track icebergs. The Synthetic Aperture Radar (SAR) data can monitor icebergs during polar night or cloudy conditions (Mazur et al., 2017; Wesche and Dierking, 2015) and are valuable datasets for detecting iceberg movements and area changes. Earlier SAR satellite data sets, such as ERS (Young et al., 1998), Envisat (Li et al., 2018; Mazur et al., 2017), and Radarsat-1 (Wesche & Dierking, 2015) have been used to study ice shelf activity. Nowadays, Sentinel-1 A/B SAR GRD data are widely used for iceberg detection due to their high temporal and spatial resolution (Torres et al., 2012; Barbat et al., 2021; Braakmann-Folgmann et al., 2021, 2022; Koo et al., 2021).

* Corresponding author

In this paper, we examine rift evolution and iceberg displacement processes associated with a major calving event in the RIS using remote sensing data from multiple sources. First, we combined multi-satellite data from 2000 to 2021 to examine the dynamic evolution of rifts at the RIS front prior to the A-76 iceberg calving event (ESA, 2021). The multi-sensor data used include optical satellite and SAR images (e.g., Landsat, Radarsat-1, ALOS, ERS, and Sentinel-1) (Table 1). Second, the Sentinel-1 A/B GRD image dataset was used to analyze the motion trajectory of the A-76 iceberg (including A-76A, A-76B and A-76C). In the following paper, we first describe the data, the study area and the subjects, then the methods for rift measurement and iceberg extraction. Finally, we present our results and draw our conclusion.

2. DATA AND STUDY SITE

Satellite data were combined to measure the rift evolution and track monitoring related to the A-76 iceberg. We obtained the RES-1, RADARSAT-1, ALOS PALSAR, and Sentinel-1 GRD satellite imagery from the Alaska Satellite Facility (<https://search.asf.alaska.edu/>) covering the RIS front between May 9, 2000, and March 11, 2022, and Landsat-7/8 imagery between February 9, 2012, and October 11, 2014 by using USGS EarthExplorer (<https://earthexplorer.usgs.gov/>). The details of the data are shown in Table 1. The study area for this paper is located in the shelf front of RIS.

Table 1. The specifications of the dataset used in this study

Data	Spatial Resolution (m)
Landsat-7 ETM+	15
Landsat 8 PAN	15
ALOS PALSAR	100
RADARSAT-1	12.5
ERS-1	12.5
Sentinel-1 GRD	20 * 40

3. METHODS

This paper examines the life cycles of the A-76 iceberg, before and after its separation from RIS to investigate the relationship between the rift evolution and iceberg calving in RIS. We observed a 21-year process from the first rift appearance, to tabular plane formation, and to final iceberg disintegration, based on images acquired from May 5, 2000 to May 13, 2021. Specifically, we analyze changes of the rifts in the shelf front of the RIS after the last major calving event in 2000 (Lazzara et al., 1999) to investigate the propagation mechanism of rifts. Then, we examined the formation of the A-76 iceberg. Finally, the drift trajectory and dynamic changes of the A-76 iceberg are analyzed (Figure 1).

	Rift measurements
Before Calving	<ul style="list-style-type: none"> • transverse rift • marginal rift • longitudinal rifts
	Iceberg Tracking
After Calving	<ul style="list-style-type: none"> • Sentinel-1 GRD image pre-processing • Iceberg Boundary Extraction • Centroid Points • A-76 (A-76A, A76-B and A-76C) iceberg drift trajectory

Figure 1. RIS rift measurements before calving and iceberg tracking after calving.

3.1 Rift Measurements and Tracking of the A-76 Iceberg

Both transverse and marginal rift propagation is involved in calving, ice front retreat, and ice shelf instability. To understand the changes in RIS rifts and its separation mechanism, we measured the lengths of transverse and marginal rifts using multi-sensor data to investigate the relationship between the rifts' changes and ice shelf calving.

To track the A-76 (A-76A, A-76B, and A-76C) iceberg, we use Sentinel-1 GRD images for edge extraction and iceberg centroid detection. First, the Sentinel images are accurately aligned, radiometrically processed, and speckle filtered; and they are then used to measure the multi-temporal parameters. Second, we segment the processed images using a multiscale segmentation method to obtain the iceberg image objects. Next, we merge these extracted segments to obtain the iceberg boundaries of the A-76 (A-76A, A-76B, and A-76C) iceberg. Then we derive the centroid coordinates from the boundaries. Finally, we use the determined centroids of the A-76 (A-76A, A-76B, and A-76C) iceberg to trace the drift trajectories. The above procedure is shown in Figure 2.

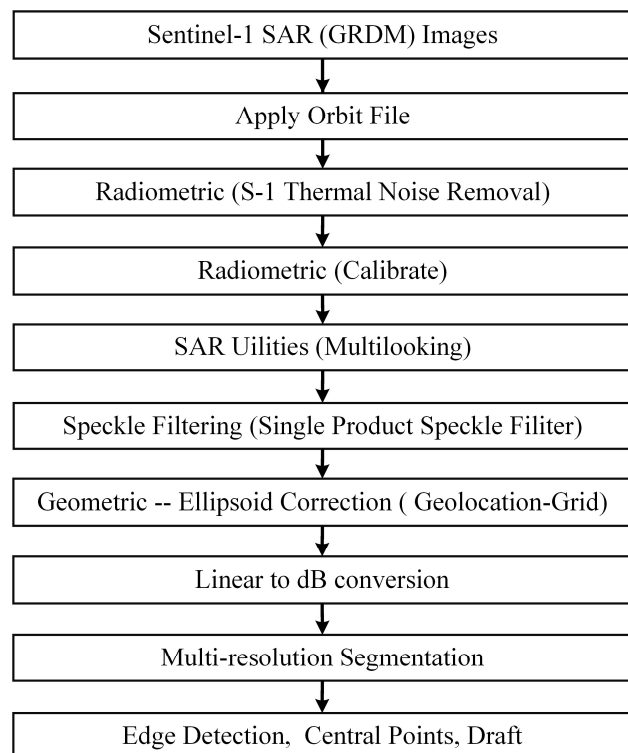


Figure 2. The workflow of A-76 (including A-76A, A-76B, and A-76C) iceberg extraction and tracking.

3.1 SAR Image Pre-processing and Multi-scale Segmentation

We obtained the Sentinel-1 GRD data from Alaska Satellite Facility (ASF) and pre-processed the data using the workflow in Figure 2. We resampled all the data to a spatial resolution of 30 m. The purpose of image segmentation in this paper is to obtain homogeneous image objects. The multi-scale segmentation method developed by Baatz & Schäpe (2000), which has also been applied to land-fast sea ice extraction in Antarctica (Kim et

al., 2020), is applied to extract boundaries of the A-76 iceberg (including A-76A, A-76B, and A-76C) from the multi-temporal SAR images. To achieve the best segmentation results, the multi-scale segmentation algorithm is a bottom-up segmentation method that minimizes the heterogeneity and maximizes the homogeneity of image objects to obtain the best segmentation results (Amani et al., 2017). The segmentation process in the multi-resolution segmentation algorithm, the segmentation process is performed according to user-defined criteria with three parameters, including the scale parameter, the weight of the shape parameter, and the weight of the compactness parameter, which are all critical to the segmentation results (Baatz & Schäpe, 2000; Belgiu & Drăguț, 2014).

The following equations (1)-(5) provide a more detailed explanation of the principles and process of segmentation. We use equation (1) to calculate the heterogeneity of the image object region (Baatz & Schäpe, 2000).

$$f = w_{color} \cdot h_{color} + (1 - w_{color}) \cdot h_{shape} \quad (1)$$

where f refers to the heterogeneity of the total area of image object. h_{color} refers to the spectral heterogeneity ranging from 0 to 1, h_{shape} refers to the shape heterogeneity ranging from 0 to 1, and w_{color} represents the weight of spectral heterogeneity.

In performing the segmentation, our goal is to obtain the best segmentation results by minimizing the heterogeneity f of image objects and maximizing the homogeneity of image objects where the spectral and shape heterogeneity are calculated using equations (2) and (3).

$$h_{color} = n_{Merge} \cdot \sigma_{Merge} - (n_{Obj1} \cdot \sigma_{Obj1} + n_{Obj2} \cdot \sigma_{Obj2}) \quad (2)$$

$$h_{shape} = w_{compact} \cdot h_{compact} + (1 - w_{compact}) \cdot h_{smooth} \quad (3)$$

where h_{smooth} refers to the smoothness, $h_{compact}$ refers to the compactness, n refers to the size of the image object, $Obj1$ and $Obj2$ represent the two smaller image objects for merging and $Merge$ represent the larger image object after connecting, and σ is the standard deviation of the spectral values within the objects.

Furthermore, the shape heterogeneity, which includes the criterion of shape smoothness and the co-determination of shape density, is calculated using (4) and (5).

$$h_{smooth} = n_{merge} \cdot \frac{l_{merge}}{b_{merge}} - \left(n_{Obj1} \cdot \frac{l_{Obj1}}{b_{Obj1}} + n_{Obj2} \cdot \frac{l_{Obj2}}{b_{Obj2}} \right) \quad (4)$$

$$h_{compact} = n_{merge} \cdot \frac{l_{merge}}{\sqrt{n_{merge}}} - \left(n_{Obj1} \cdot \frac{l_{Obj1}}{\sqrt{n_{Obj1}}} + n_{Obj2} \cdot \frac{l_{Obj2}}{\sqrt{n_{Obj2}}} \right) \quad (5)$$

where l refers to the perimeter of the image object, and b refers to the outer tangential rectangle of image object. Throughout the segmentation process, the whole image is segmented. The scale parameters affect the average size of the image objects, which are generated according to several adjustable homogeneities or heterogeneity criteria for h_{shape} and h_{color} .

This study tested various combinations of weights for the scale, shape, and compactness parameter fields, and an optimized combination was determined based on a visual inspection of the resulting objects. We employed the control variable method for parameter selection to get better segmentation parameters. To begin the experiment, we set the compactness parameter to 0.5, the shape parameters to 0.1, 0.3, and 0.5, and the segmentation scales to 100, 300, 500, 800, and 1000, for a total of 15-parameter combinations. In the segmentation experiments, these three parameters interact with one another. To control the segmentation quality, over-segmentation is checked in Figure 3 (a) and (b), and under-segmentation as shown in Figures 3 (c) and (d). Over- and under-segmentation problems are avoided by controlling the level of details based on appropriate scale values. The smaller value of the scale parameter, the smaller the resulting object, and vice versa. Smaller shape values produced better segmentation results, as shown in Figure 3 (a) (b), as well as Figure 3 (c) (d).

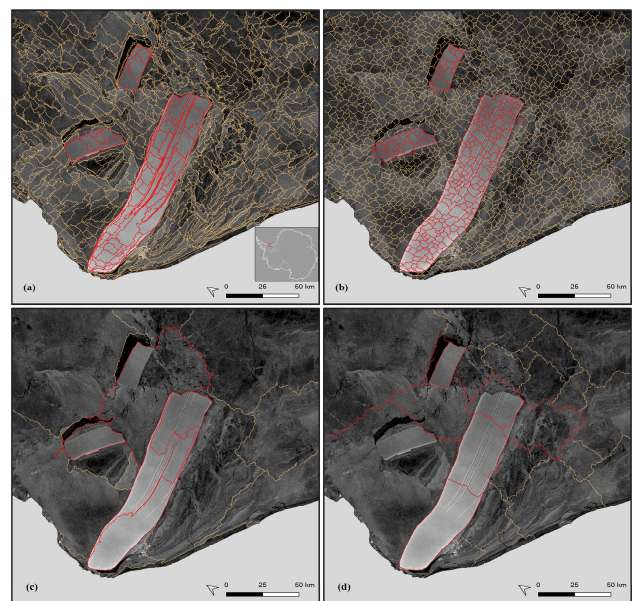


Figure 3. Examples of segmentation results with the compactness parameter set to 0.5 in all experiments: (a) a scale parameter of 100 with a fixed threshold of 0.1 for shape parameter, (b) a scale of 100 with shape parameter for 0.5, (c) a scale parameter of 800 with the shape parameter for 0.1, and (d) a scale parameter of 800 with a shape parameter of 0.5. The brown lines demarcate the image object boundaries of the background and the red lines contain iceberg boundaries. The location of the study area is shown in the inset of Figure 3(a).

We found that a scale threshold of 500 produces a clear and reasonable segmentation of the iceberg's boundary, and that using smaller shape values produced better segmentation results. The A-76 iceberg (containing A-76A, A-76B, and A-76C) can be extracted well when the segmentation scale is 500, the shape parameter is 0.1, and the compactness parameter is 0.5. Figure 4 shows the segmentation results of the Sentinel-1 GRD image collected on July 3, 2021.

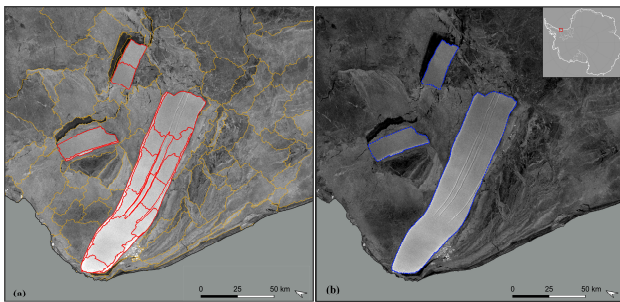


Figure 4. (a) The brown lines demarcate the image object boundaries, and the red lines show the A-76 iceberg boundaries (including A-76A, A-76B, and A-76C). (b) The iceberg borders of A-76A, A-76B, and A-76C are shown by blue dashed lines. Sentinel-1 GRD image data collected on July, 3 2021 in the background.

3.2 Iceberg's Centroid Computation

The iceberg's boundary is determined by the result of the preceding segmentation stage. Using equations (6) and (7), we extract the object centroid from the retrieved A-76, A-76A, A-76B, and A-76C icebergs, and then derive the coordinates of the iceberg's centroid points (\bar{j}_i, \bar{k}_i). The following are the details of equations (6) and (7) (Moctezuma-Flores & Parmiggiani, 2017).

$$\bar{j}_i = \frac{1}{A_i} \sum_{j=1}^M \sum_{k=1}^N j O_i(j, k) \quad (6)$$

$$\bar{k}_i = \frac{1}{A_i} \sum_{j=1}^M \sum_{k=1}^N k O_i(j, k) \quad (7)$$

$O_i(j, k)$ refers to the object containing the icebergs, i refers to different icebergs, A_i refers to the iceberg area, j and k refer to rows and columns, and M and N represent the area of the object icebergs in the above equations.

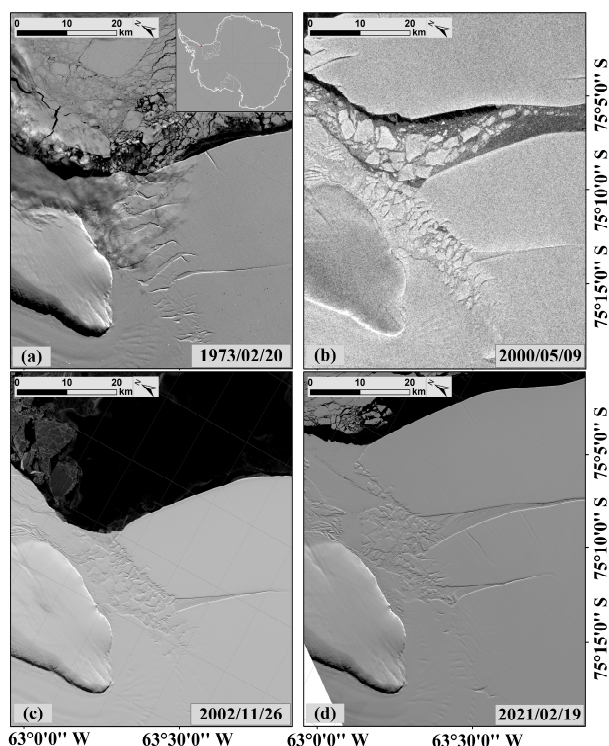


Figure 5. Fracture features in Landsat and Radarsat-1 images of RIS front collected on February 20, 1973, May 9, 2000, November 26, 2002, and December 19, 2021, are shown in (a), (b), (c) and (d) respectively.

4. RESULTS

4.1 Rifts Changes

In the shear margin of RIS has always been occupied by marginal rifts at difference evolution stages (Figure 5a and 5b). Marginal rifts may increase their lengths in the lateral directions to connect to transverse rifts and form calving blocks (Lazzara et al., 1999). At same time they also break to fragments and produce mélanges. Figure 5 (c) and (d) show how the marginal rift changed from 2002 to 2021, that contributed to the major calving in RIS occurred eventually on May 13, 2021.

The transverse rifts, marginal rifts, and longitudinal rifts each accounted for 46.5%, 39.9%, and 13.6%, respectively, of the detachment boundary of the A-76 iceberg to complete the calving process. The long transverse rift (270 km) is one of the rifts defined as dormant or intermittently active by Walker and Gardner (2019) and Hulbe et al. (2010).

The RIS marginal rifts formed rapidly as warm Southern Ocean interacted with the shelf front, forming dynamic regions in the shear margins filled with mélanges. The major marginal faults have evolved dramatically over the last decade and are now poised to join the transverse rifts. We used multi-sensors data to analyze the pre-calving rift development process and iceberg characteristics, including optical satellite and Synthetic Aperture Radar (SAR) images (e.g., Landsat, Radarsat-1, ALOS, ERS, and Sentinel-1) (Table 1). The transverse rift grew slowly, expanding 16.1 km over last 20 years, with 17% of the growth occurring in 2000. It is worth noting that the growth of the marginal rift has occurred in two stages. It grew by 16.5 km between May 2000 and January 2018, at a rate of 0.9 km/y. The rifts suddenly expanded to 72.6 km in the second period, from January to December 2018, at a rate of 43.7 km/y (Figure 6). Finally, in December 2018, the active margin rift reached the transverse rift.

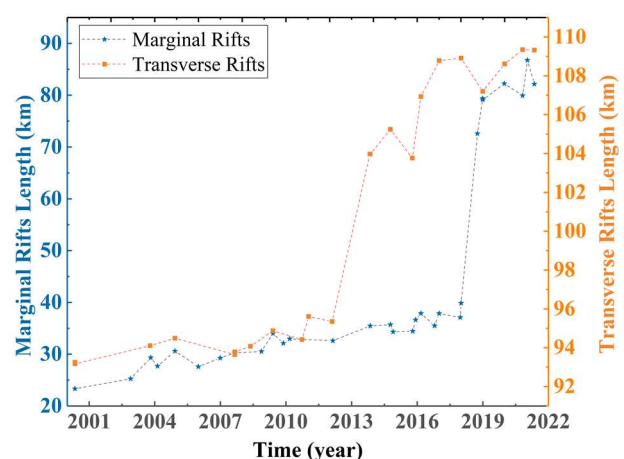


Figure 6. The length of rifts has changed over time, from 2000 to 2022. The left axis represents changes in the development of marginal rifts (blue), while the right axis represents changes in the development of transverse rifts (orange).

4.2 A-76 Iceberg Tracking from Space

A-76 iceberg entered the Weddell Sea from RIS on May 13, 2021, as observed by the British Antarctic Survey and confirmed by the United States National Ice Centre using Copernicus (Figure 7, ESA, 2021); the A-76 iceberg has a total area of 4320 km². Thirteen days later, the iceberg was further divided into three sections, A-76A, A-76B, and A-76C (USNIC, 2021), each with areas of 3442 km², 479 km², and 400 km². The entire calving process of A-76 iceberg was captured by Sentinel-1 GRD images from May 11, two days before calving, to May 26 (Figure 7).

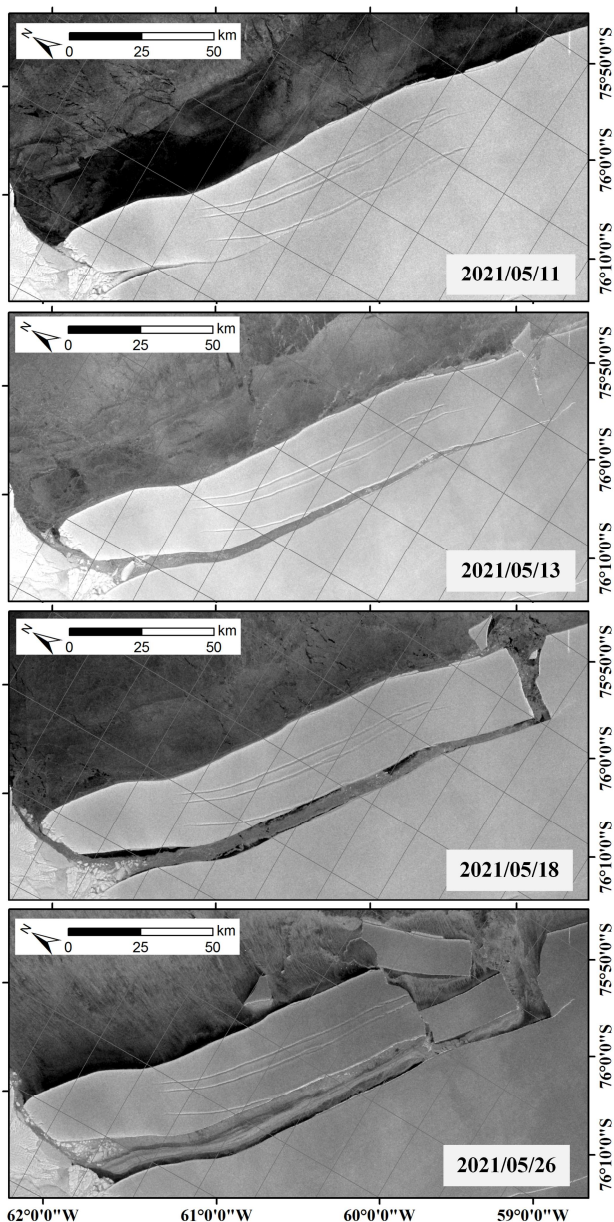


Figure 7. The RIS front area before (a), and after (b), (c) and (d), the detachment of the iceberg in May 2021.

Figure 8 depicts the drift trajectory of each iceberg. The extracted centroids and Eulerian paths are color coded, with blue indicating the centroid of the extracted A-76 iceberg and the corresponding blue solid line. From May 14, 2021 to May 25, 2021, the A-76 iceberg is relatively stable, and moving at an average speed of 0.89 km/d. The A-76A, A-76B, and A-76C icebergs are represented by the orange, light blue, and green, respectively.

Table 2 displays the travelled Eulerian distances and mean velocities of the icebergs calculated from the Sentinel-1 image pairs. The Eulerian distance for A-76 iceberg over 13 days is 9.83 km. The travelled Eulerian distance of A-76A, A-76B, and A-76C icebergs over 289 days (from May 26 2021 to March 11, 2022) are 647.08 km, 405.46 km, and 775.05 km, respectively. The A-76C iceberg drifted the fastest, followed by A-76A and A-76B. Their velocities are 2.57 km/d, 2.14 km/d, and 1.34 km/d, respectively, from May 26, 2021 to March 11, 2022, and the details of the results are shown in Table 2. As the icebergs drift through the ocean, their position and orientation change over time. We hypothesize that the varying trajectories and velocities of A-76A, A-76B, and A-76C icebergs are caused by a variety of complex environmental variables (e.g., ocean currents, winds, seafloor topography, atmosphere, and sea ice) (Li et al., 2018; Koo et al., 2021).

Table 2. Relative displacements and velocities of the A-76, A-76A, A-76B, and A-76C icebergs derived from the image dataset.

Name	Distance traveled (km)	Velocity (km/d)
A76	9.83	0.89
A-76A	647.08	2.14
A-76B	405.46	1.34
A-76C	775.05	2.57

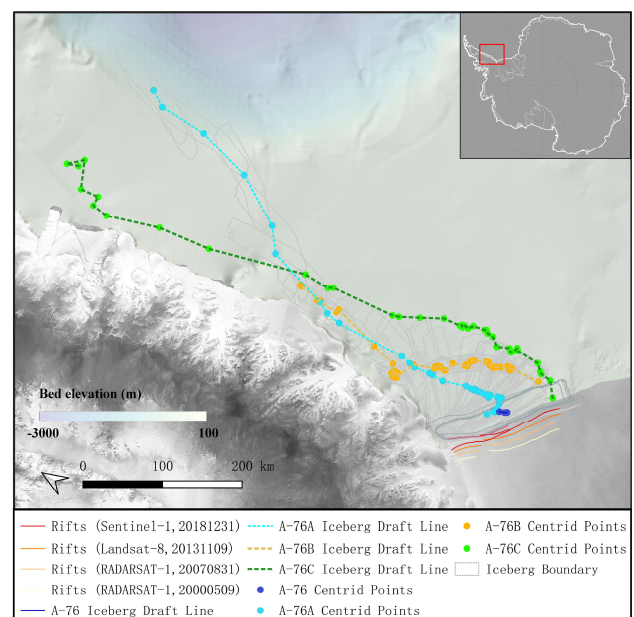


Figure 8. The motion trajectories of three icebergs from May 13, 2021 to March 11, 2022. The A-76, A-76A, A-76B, and A-76C icebergs trajectories overlaid with bed elevation data from BedMachine Antarctica (Morlighem et al., 2020).

5. CONCLUSIONS

The final evolution process of the iceberg producing rifts of A-76 in RIS is investigated in this study, specifically the variation in rift length before calving and the iceberg's drift trajectory after calving. First, we tracked the changes in the rifts near the RIS's shelf front. The findings show that transverse rifts at the RIS shelf front determine iceberg size and develop relatively slowly, whereas marginal rifts develop at a faster rate before calving. The interconnection of transverse and marginal rifts may provided a high probability of a short term iceberg disintegration. Second,

we developed a semi-automatic method for calculating the trajectories of A-76, A-76A, A-76B, and A-76C icebergs from the Sentinel-1 A/B GRD image data. Our findings can also be used to model the break-up of other large tabular icebergs that follow similar paths, and their effects can be incorporate into ocean models. We will also optimize our methodology to monitor additional parameters such as iceberg area, thickness, freeboard, and volume to assess the rate of iceberg melting. Additionally, we may also study the effect of air temperature, ocean temperature, wind speed, and seafloor topography on the drift, area change, and ice volume change of A-76A, A-76B, and A-76C icebergs.

Disclosure Statement

No potential conflict of interest was reported by the authors.

Author contributions

RL led the study and created the research concept. AZ developed the method and processed the data, YC analyzed the data and LA interpreted results and edited the entire manuscript. Everyone is involved in background research for this project.

ACKNOWLEDGEMENTS

This study was supported by the National Science Foundation of China (41730102). We greatly acknowledge the use of imagery from ESA (available via <https://search.asf.alaska.edu>), USGS (available via <https://earthexplorer.usgs.gov/>).

REFERENCES

- Amani, M., Salehi, B., Mahdavi, S., Granger, J., & Brisco, B. (2017). Wetland classification in Newfoundland and Labrador using multi-source SAR and optical data integration. *GIScience & Remote Sensing*, 54, 779–796. <https://doi.org/10.1080/15481603.2017.1331510>
- Barbat, M. M., Rackow, T., Wesche, C., Hellmer, H.H., & Mata, M.M. (2021). Automated iceberg tracking with a machine learning approach applied to SAR imagery: A Weddell Sea case study. *ISPRS Journal of Photogrammetry and Remote Sensing*, 172: 189–206. <https://doi.org/10.1016/j.isprsjprs.2020.12.006>
- Baatz, M., & Schäpe, A. (2000). Multiresolution segmentation—an optimization approach for high quality multi-scale image segmentation. J. Strobl, T. Blaschke, G. Griesebner (Eds.), *Angew. Geogr. Info. verarbeitung*, Wichmann Verlag, Heidelberg (2000), pp. 12–23
- Belgiu, M., & Drăguț, L. (2014). Comparing supervised and unsupervised multiresolution segmentation approaches for extracting buildings from very high resolution imagery. *ISPRS Journal of Photogrammetry and Remote Sensing*, 96, 67–75. <https://doi.org/10.1016/j.isprsjprs.2014.07.002>
- Braakmann-Folgmanna, A., Shepherd, A., & Ridout, A. (2021). Tracking changes in the area, thickness, and volume of the Thwaites tabular iceberg “B30” using satellite altimetry and imagery. *The Cryosphere*, 15, 3861–3876. <https://doi.org/10.5194/tc-15-3861-2021>
- Braakmann-Folgmanna, A., Shepherd, A., Gerrish, L., Izzard, J., & Ridout, A. (2022). Observing the disintegration of the A68A iceberg from space. *Remote Sensing of Environment*, 270, 112855. <https://doi.org/10.1016/j.rse.2021.112855>
- Cheng, Y., Xia, M., Qiao, G., Lv, D., Li, Y., & Hai, G. (2021). Imminent calving accelerated by increased instability of the Brunt Ice Shelf, in response to climate warming. *Earth and Planetary Science Letters*, 572, 117132. <https://doi.org/10.1016/j.epsl.2021.117132>
- Collares, L. L., Mata, M.M., Kerr, R., Arigony-Neto, J., & Barbat, M.M. (2018). Iceberg drift and ocean circulation in the northwestern Weddell Sea, Antarctica. *Deep-Sea Res. Pt. II*, 149, 10–24. <https://doi.org/10.1016/j.dsr2.2018.02.014>
- ESA. (2021). A-76: The world's largest iceberg. https://www.esa.int/ESA_Multimedia/Images/2021/05/Meet_the_world_s_largest_iceberg (last access: March 30, 2022).
- USNIC. (2021). Iceberg A-76 Calves from the Ronne Ice Shelf in the Weddell Sea, Largest Iceberg in the World. U.S. National Ice Center, May 26, 2021., https://usicecenter.gov/PressRelease/IcebergA76A_B_C (last access: March 30, 2022).
- Fricker, H.A., Young, N.W., Coleman, R., Bassis, J.N., & Minster, J.B. (2005). Multi-year monitoring of rift propagation on the Amery Ice Shelf, East Antarctica. *Geophysical Research Letters*, 32(2), L02502. <https://doi.org/10.1029/2004gl021036>
- Gudmundsson, G. H. (2013). Ice-shelf buttressing and the stability of marine ice sheets. *The Cryosphere*, 7, 647–655. <https://doi.org/10.5194/tc-7-647-2013>
- Hulbe, C. L., LeDoux, C., & Cruikshank, K. (2010). Propagation of long fractures in the Ronne Ice Shelf, Antarctica, investigated using a numerical model of fracture propagation. *Journal of Glaciology*, 56(197), 459–472. <https://doi.org/10.3189/002214310792447743>
- Kim, M., Kim, H.-C., Im, J., Lee, S., & Han, H. (2020). Object-based landfast sea ice detection over West Antarctica using time series ALOS PALSAR data. *Remote Sensing of Environment*, 242, 111782. <https://doi.org/10.1016/j.rse.2020.111782>
- Koo, Y., Xie, H., Ackley, S. F., Mestas-Nuñez, A. M., Macdonald, G. J., & Hyun, C. U. (2021). Semi-automated tracking of iceberg B43 using Sentinel-1 SAR images via Google Earth Engine. *The Cryosphere*, 15, 4727–4744. <https://doi.org/10.5194/tc-15-4727-2021>
- Larour, E., Rignot, E., Poinelli, M., & Scheuchl, B. (2021). Physical processes controlling the rifting of Larsen C Ice Shelf, Antarctica, prior to the calving of iceberg A68. *Proceedings of the National Academy of Sciences* 118(40): e2105080118. <https://doi.org/10.1073/pnas.2105080118>
- Lasserre, F. (2015). Simulations of shipping along Arctic routes: comparison, analysis and economic perspectives. *Polar Record*, 51(3), 239–259. <https://doi.org/10.1017/S0032247413000958>
- Lazzara, M. A., Jezek, K. C., Scambos, T. A., MacAyeal, D. R., & van der Veen, C. J. (1999). On the recent calving of icebergs from the Ross Ice Shelf. *Polar Geography*, 23:3, 201–212. <https://doi.org/10.1080/10889379909377676>
- Li, R., Xiao, H., Liu, S., & Tong, X. (2017). A Systematic Study of the Fracturing of Ronne - Filchner Ice Shelf, Antarctica, Using Multisource Satellite Data from 2001 to 2016. *The Cryosphere*

Discuss. [preprint], <https://doi.org/10.5194/tc-2017-178>

Li, T., Shokr, M., Liu, Y., Cheng, X., Li, T., Wang, F., & Hui, F. (2018), Monitoring the tabular icebergs C28A and C28B calved from the Mertz Ice Tongue using radar remote sensing data. *Remote Sensing of Environment.*, 216, 615–625, <https://doi.org/10.1016/j.rse.2018.07.028>

Moctezuma-Flores, M., & Parmiggiani, F. (2017). Tracking of the iceberg created by the Nansen Ice Shelf collapse. *International Journal of Remote Sensing*, 38:5, 1224-1234. <https://doi.org/10.1080/01431161.2016.1275054>

Mazur, A. K., Wåhlin, A. K., & Krężel, A. (2017), An object-based SAR image iceberg detection algorithm applied to the Amundsen Sea. *Remote Sensing of Environment.*, 189, 67–83. <https://doi.org/10.1016/j.rse.2016.11.013>

Morlighem, M., Rignot, E., Binder, T., Blankenship, D., Drews, R., Eagles, G., Eisen, O., Ferraccioli, F., Forsberg, R., Fretwell, P., Goel, V., Greenbaum, J. S., Gudmundsson, H., Guo, J., Helm, V., Hofstede, C., Howat, I., Humbert, A., Jokat, W., Karlsson, N. B., Lee, W. S., Matsuoka, K., Millan, R., Mouginit, J., Paden, J., Pattyn, F., Roberts, J., Rosier, S., Ruppel, A., Seroussi, H., Smith, E. C., Steinhage, D., Sun, B., van den Broeke, M. R., van Ommen, T. D., van Wessem, M., & Young, D. A. (2020). Deep glacial troughs and stabilizing ridges unveiled beneath the margins of the Antarctic ice sheet. *Nature Geoscience.*, 13, 132–137. <https://doi.org/10.1038/s41561-019-0510-8>

Paolo, F.S., Fricker, H.A., & Padman, L. (2015). Volume loss from Antarctic ice shelves is accelerating. *Science* 348, 327-331. <https://doi.org/10.1126/science.aaa0940>

Rignot, E., Jacobs, S., Mouginit, J., & Scheuchl, B. (2013). Ice-Shelf Melting Around Antarctica. *Science*, 341(6143), 266–270. <https://doi.org/10.1126/science.1235798>

Torres, R., Snoeij, P., Geudtner, D., Bibby, D., Davidson, M., Attema, E., Potin, P., Rommen, B. Ö., Floury, N., Brown, M., Traver, I. N., Deghaye, P., Duesmann, B., Rosich, B., Miranda, N., Bruno, C., L'Abbate, M., Croci, R., Pietropaolo, A., Huchler, M., & Rostan, F. (2012). GMES Sentinel-1 mission. *Remote Sensing of Environment.*, 120, 9–24. <https://doi.org/10.1016/j.rse.2011.05.028>

Walker, C. C., & Gardner, A.S. (2019). Evolution of ice shelf rifts: Implications for formation mechanics and morphological controls. *Earth and Planetary Science Letters.*, 526(15):115764. <https://doi.org/10.1016/j.epsl.2019.115764>

Walker, C. C., Bassis, J. N., & Fricker, H. A., Czerwinski, R. J. (2015). Observations of interannual and spatial variability in rift propagation in the Amery Ice Shelf, Antarctica, 2002–14. *Journal of Glaciology*, 61(226), 243–252. <https://doi.org/10.3189/2015JoG14J151>

Walker, C. C., Bassis, J. N., Fricker, H. A., & Czerwinski, R. J. (2013). Structural and environmental controls on Antarctic ice shelf rift propagation inferred from satellite monitoring. *Journal of Geophysical Research: Earth Surface*, 118(4), 2354-2364. <https://doi.org/10.1002/2013JF002742>

Wesche, C. & Dierking, W. (2015). Near-coastal circum-Antarctic iceberg size distributions determined from Synthetic Aperture Radar images. *Remote Sensing of Environment.*, 156, 561–569. <https://doi.org/10.1016/j.rse.2014.10.025>

Young, N. W., Turner, D., Hyland, G., & Williams, R. N. (1998). Near-coastal iceberg distributions in East Antarctica, 50–145° E. *Annals of Glaciology.*, 27, 68–74. <https://doi.org/10.3189/1998aog27-1-68-74>